



## Absence of a strong, deep-reaching Antarctic Circumpolar Current zonal flow across the Tasmanian gateway during the Oligocene to early Miocene

Dimitris Evangelinos<sup>a,b,\*</sup>, Carlota Escutia<sup>b</sup>, Tina van de Flierdt<sup>c</sup>, Luis Valero<sup>d</sup>, José-Abel Flores<sup>e</sup>, David M. Harwood<sup>f</sup>, Frida S. Hoem<sup>g</sup>, Peter Bijl<sup>g</sup>, Johan Etourneau<sup>a,h</sup>, Katharina Kreissig<sup>c</sup>, Katrina Nilsson-Kerr<sup>i</sup>, Liam Holder<sup>c</sup>, Adrián López-Quirós<sup>j,b</sup>, Ariadna Salabarnada<sup>b</sup>

<sup>a</sup> UMR 5805 EPOC CNRS, University of Bordeaux, Bordeaux, France

<sup>b</sup> Instituto Andaluz de Ciencias de la Tierra, CSIC-Univ. de Granada, Av. de las Palmeras, 4, 18100 Armilla, Spain

<sup>c</sup> Department of Earth Sciences and Engineering, South Kensington Campus, London SW7 2AZ, United Kingdom

<sup>d</sup> Département des Sciences de la Terre, Université de Genève, Rue des Marchers 13, 1205 Geneva, Switzerland

<sup>e</sup> Department of Geology, University of Salamanca, 37008 Salamanca, Spain

<sup>f</sup> Earth & Atmospheric Sciences, University of Nebraska, Lincoln, Lincoln, NE, USA

<sup>g</sup> Palaeoecology, Institute of Environmental Biology, Faculty of Science, Laboratory of Palaeobotany and Palynology, Utrecht, University, Budapestlaan, 4, 3584 CD Utrecht, the Netherlands

<sup>h</sup> EPHE, PSL University, Paris, France

<sup>i</sup> School of Environment, Earth and Ecosystem Sciences, Faculty of Science, Technology, Engineering and Mathematics, The Open University, Milton, Keynes, United Kingdom

<sup>j</sup> Department of Geoscience, Aarhus University, Høegh-Guldbergs Gade 2, 8000 Aarhus C, Denmark

### ARTICLE INFO

Editor: Howard Falcon-Lang

#### Keywords:

ACC  
CDW  
Neodymium isotope ratios  
Deep ocean circulation  
Tasmanian Gateway  
Oligocene-early Miocene

### ABSTRACT

The vigorous eastward flow of the Antarctic Circumpolar Current (ACC) connects all major ocean basins and plays a prominent role in the transport of heat, carbon and nutrients around the globe. However, the establishment of a deep circumpolar flow, similar to the present-day ACC, remains controversial thereby obscuring our understanding of its climatic impact. Deciphering the chemical composition of Circumpolar Deep Water (CDW) within the ACC can provide critical insights about its development and evolution. Here we present new fossil fish teeth/bone debris neodymium isotope ( $\epsilon_{Nd}$ ) records from Deep Sea Drilling Project (DSDP) Sites 278 and 274 in the southwest Pacific Ocean, with the aim to trace changes in deep water masses across the Tasmanian Gateway between the early Oligocene and early Miocene (~ 33–22 Ma). Site 274 provides the first Nd isotope record proximal to the Ross Sea during the Oligocene (33.5–23.4 Ma). Its Nd isotope composition shows excursions to very radiogenic values,  $\epsilon_{Nd(t)} = -3.1$  and  $\epsilon_{Nd(t)} = -3.7$ , at 33.5 Ma and 23.8 Ma, respectively, in response to major steps in Antarctic ice sheet expansion. A shift to lower, more unradiogenic  $\epsilon_{Nd(t)}$  values between 29.7 and 29.1 Ma is linked to an increased influence of proto-CDW upwelling at the site. In contrast, the Nd isotope record from Site 278 in the southern Emerald Basin shows little variability ( $\epsilon_{Nd(t)} = -6.0$  to  $-6.7$ ) throughout the Oligocene and early Miocene (30.9–21.8 Ma). Comparison with published data north of the ACC path, demonstrates the presence of two deep water masses in the South Pacific prior to the inferred onset of the ACC (33–30 Ma), one occupying depths between ~2500 and 3000 m ( $\epsilon_{Nd(t)} \sim -3$  to  $-5$ ) and a deep/bottom water mass (> 3000 m) with a more unradiogenic Nd isotope composition ( $\epsilon_{Nd(t)} \sim -6$ ). Site 278 located close to the proto-polar front (proto-PF) indicates that following the inferred onset of the ACC, deep waters bathing the southern Emerald Basin remained more radiogenic in the Southwest Pacific compared to sites along the proto-PF in the South Atlantic and Indian Ocean ( $\epsilon_{Nd(t)} \sim -8.1$ ). This indicates a provinciality in Nd isotope compositions of deep waters along the proto-PF across the Tasmanian Gateway. Our data are incompatible with the existence of a modern-like homogenous (lateral and vertical) Nd isotope composition of CDW along the main flow path of the ACC in all oceanic basins in the Oligocene to early Miocene. We attribute distinct Nd isotope compositions of deep waters across the Tasmanian Gateway to reflect a less deep reaching and weaker ACC (proto-ACC) than

\* Corresponding author at: UMR 5805 EPOC CNRS, University of Bordeaux, Bordeaux, France.

E-mail address: [dimitrios.evangelinos@u-bordeaux.fr](mailto:dimitrios.evangelinos@u-bordeaux.fr) (D. Evangelinos).

<https://doi.org/10.1016/j.gloplacha.2021.103718>

Received 18 December 2020; Received in revised form 20 October 2021; Accepted 26 November 2021

Available online 3 December 2021

0921-8181/© 2021 Elsevier B.V. All rights reserved.

today. Our findings suggest that the modern strong and deep-reaching ACC flow must have been developed at a later point in the Neogene.

## 1. Introduction

The Antarctic Circumpolar Current (ACC) is the world's largest and strongest ocean current, transporting  $\sim 136\text{--}162 \times 10^6 \text{ m}^3 \text{ s}^{-1}$  of water along a  $\sim 20,000$  km long path around Antarctica (e.g., Rintoul et al., 2014). The absence of continental barriers around  $60^\circ\text{S}$  permits the vigorous eastward flow of the ACC, which is driven by the strong westerly winds (westerlies) and buoyancy forcing (Rintoul, 2018). Most of the circumpolar flow of the ACC takes place along the Polar and the Subantarctic Fronts (PF and SAF, respectively), which extend from the surface to the seafloor (i.e. deep-reaching), connecting the Atlantic, Pacific and Indian Oceans, thus actively modulating the global ocean circulation (Orsi et al., 1995; Sokolov and Rintoul, 2007; Rintoul, 2018). This interbasin connection of the ACC is a critical feature of the modern global overturning circulation, which carries heat, carbon and nutrients around the globe. It modulates the exchange of heat, moisture and carbon dioxide ( $\text{CO}_2$ ) between the ocean and the atmosphere and controls local and global marine primary productivity (Rintoul, 2018).

Despite the critical role of today's strong deep-reaching ACC flow in the global ocean circulation and Earth's climate, there is still an ongoing debate regarding the timing of its onset and evolution towards a modern-like configuration throughout the Cenozoic period. Major changes in paleogeography and seafloor paleobathymetry related to tectonic activity through time, as well as changes in climate are likely to have controlled the initiation and evolution of the ACC during the Cenozoic. For example, it is widely accepted that the ACC only initiated after the opening of the two last major land barriers within its circum-Antarctic flow, the Drake Passage and the Tasmanian Gateway, and their respective deepening to bathyal depths ( $>2000$  m). Dating the time when the Drake Passage reached this depth is controversial, spanning from the middle Eocene to the late Miocene (see Dalziel, 2014 for discussion). In contrast, the opening of the Tasmanian Gateway is better constrained (Stickley et al., 2004).

A Southern Ocean with closed tectonic gateways featured clockwise gyres in the South Pacific and South Indian/Atlantic Ocean basins (Huber et al., 2004). Between  $\sim 49$  Ma and 35.5 Ma, a shallow current flowing westward across the Tasmanian Gateway (from the Pacific to the Indian Ocean) was proposed based on marine microfossils, organic geochemical records and model simulations (Huber et al., 2004; Bijl et al., 2013). Initial opening was followed by intensified deepening of the seaway between  $\sim 35.5$  and 30.2 Ma as indicated by the analysis of sedimentological, micropaleontological and paleomagnetic data (Stickley et al., 2004). Chemical water mass reconstructions suggest a westward flowing (i.e., from the Pacific to the Indian Ocean) deep water current connecting both sides of the northern parts of the Tasmanian Gateway between 32 and 30 Ma (Scher et al., 2015). A deep eastward flowing water connection between the Indian and Pacific sectors of the Southern Ocean, was only established after 30 Ma, probably due to alignment of the northern part of the Tasmanian Gateway within the latitudinal band of the westerlies (Scher et al., 2015). However, micropaleontological and paleotemperature records suggest weak latitudinal paleotemperature gradients and warm conditions prevailed in the Southern Ocean until at least the mid-Miocene (Bijl et al., 2018; Hartman et al., 2018; Salabarnada et al., 2018; Sangiorgi et al., 2018). Thus, the characteristics of this nascent ACC remain poorly understood.

One possible way to reconstruct past connectivity along the ACC is to track the evolution of Circumpolar Deep Water (CDW), using neodymium (Nd) isotope compositions ( $^{143}\text{Nd}/^{144}\text{Nd}$  ratio) of ambient seawater in fossil fish teeth and bones (e.g., Wright et al., 2018). Circumpolar Deep Water is the most voluminous water mass in the Southern Ocean, occupying the shallow to deep layers of the ACC in the Southern Ocean

(Orsi et al., 1995). Today, CDW has a vertically and horizontally homogeneous Nd isotope composition, probably due to the strong vertical and horizontal mixing along the frontal systems (e.g., Stichel et al., 2012; Lambelet et al., 2018). These findings indicate that the evolution of the Nd isotope composition of CDW in the past may provide important insights into interbasinal connections/circulation in the Southern Ocean.

Neodymium is incorporated into fish teeth at the sediment-water interface at the time of deposition, remineralisation and burial (Martin and Haley, 2000). Post-burial alteration is generally negligible relative to the early diagenetic rare earth element (REE) uptake, allowing retention of the Nd isotope composition of bottom water signals (e.g., Martin and Haley, 2000). Neodymium is a lithogenic element, introduced to the ocean at its interfaces with the solid earth (e.g., van de Flierdt et al., 2016). Water masses forming in the different oceanic basins are distinct in their Nd isotope fingerprint, due to the distribution of geological ages and lithologies around the globe, with younger volcanic material yielding more radiogenic (higher) Nd isotope compositions, and older cratonic rocks being characterised by less radiogenic (lower) Nd isotope compositions.  $\epsilon_{\text{Nd}}$  denotes the deviation of a measured  $^{143}\text{Nd}/^{144}\text{Nd}$  ratio from the chondritic uniform reservoir in parts per 10,000 (Jacobsen and Wasserburg, 1980). Because seawater Nd has a relatively short residence time in the ocean ( $\sim 500$  to 1000 years) (Tachikawa et al., 2003), Nd can be carried from one ocean basin to another, and hence trace the provenance of water masses.

Here we present new Oligocene to lower Miocene neodymium isotope data obtained from fossil fish teeth and bones (fish debris) in sediments recovered by the Deep Sea Drilling Project (DSDP) at Sites 278 and 274. Site 278 is strategically located within the main path of the modern ACC in the southern Emerald Basin (Kennett et al., 1975; Rintoul et al., 2014), while Site 274 is situated proximal to the Ross Sea in the Adare Basin (Figs. 1A; 1B; S1) (Hayes and Frakes, 1975). Our new data provide critical insights into the chemical evolution of CDW in the Southwest Pacific in the time period following the initial (northern) opening of the Tasmanian Gateway and leading up to the development of the modern-like ACC.

## 2. Modern oceanographic setting of drill sites DSDP 274 and 278

To study the history of the ACC, and particularly the chemical composition of deep waters through the Oligocene to early Miocene, we used sediments recovered from Hole 278 (Kennett et al., 1975). Site 278 ( $56^\circ 33.42'\text{S}$ ,  $160^\circ 04.29'\text{E}$ , 3675 m water depth) is located on a pelagic contourite drift in the southern Emerald Basin (Figs. 1A; 1B) (Kennett et al., 1975). At present, the site is located close to the northern branch of the Polar Front (PF) and within the main pathway of the ACC (Sokolov and Rintoul, 2007; Rintoul et al., 2014). As the ACC enters the Southwest Pacific through the Tasmanian Gateway, its flow is constrained by the Macquarie Ridge, which extends from depths of 5000 m to an average depth of 1500 m between  $47^\circ\text{S}$  and  $56^\circ\text{S}$  (Rintoul et al., 2014). The ACC passes over and through narrow gaps of the Macquarie Ridge and south of the ridge crest around  $56^\circ\text{S}$ , before reaching the southern Emerald Basin (Rintoul et al., 2014). From there, the ACC flows around the southern edge of the Campbell Plateau and to the Bounty Trough, reinforcing the Deep Western Boundary Current (DWBC). South of the Bounty Trough ( $46^\circ\text{S}$ ) the ACC turns to the east and continues its journey across the South Pacific, while the DWBC continues north towards the equator in the Pacific Ocean basin (Carter and McCave, 1997). The ACC carries CDW eastwards from the Southeast Indian Ocean into the Southwest Pacific Ocean. In the modern southern Emerald Basin, CDW extends to the seafloor, bathing Site 278 (Figs. 1B; S1-S2) (Rintoul et al.,

2014; Lambelet et al., 2018).

Site 274 (68°59.81'S, 173°25.64'E, 3305 m water depth) was drilled on the lower continental rise, 250 km north-northeast of Cape Adare (Hayes and Frakes, 1975) (Fig. 1B). It is currently situated south of the Southern ACC Front (SACCF) (Figs. 1B; S1) (Sokolov and Rintoul, 2007) and within the main outflow path of bottom water formed in the western Ross Sea (Gordon et al., 2009). At a depth of 3305 m, the main modern water mass encountered is Ross Sea Bottom Water (RSBW) (Fig. 1B; S1). Today, most of the dense shelf water on the Ross Sea shelf resides in the Joides and Drygalski troughs, from where it is exported as RSBW to the abyssal plains (Fig. 1B) (Gordon et al., 2009). In contrast to CDW, which can be found all around Antarctica, bottom topography restricts the pathway of the Antarctic Bottom Water (AABW), including RSBW, in the Southern Ocean (Orsi et al., 1995). Only a small portion of RSBW formed in the western Ross Sea flows northward from its outlets, with most of it being diverted westward against the continental slope into the deep Australian-Antarctic Basin (Gordon et al., 2009). Through diapycnal mixing with overlying CDW, the hydrographic properties of RSBW quickly erode along its westward pathway and are only detectable to ~140°E along the Adélie-Wilkes Coast (Rintoul, 1998). In contrast, there is a larger fraction of RSBW detected north of the Ross Sea, but this variety of RSBW forms predominantly in the central Ross Sea and is channelled to the continental slope by the Glomar Challenger trough and into the Hillary Canyon. Much of this bottom water enters the southeast Pacific Basin (Fig. 1B) (Gordon et al., 2009).

### 2.1. Modern Nd isotope signatures of deep and bottom waters around the Tasmanian Gateway

Globally, North Atlantic Deep Water (NADW) and Pacific Deep Water (PDW) constitute water mass endmembers in terms of their Nd isotope composition. Modern NADW is characterised by relatively negative  $\epsilon_{Nd}$  values ( $\epsilon_{Nd} \sim -12$  to 13) (e.g., Lambelet et al., 2016), resulting from the weathering of old cratonic rocks surrounding the

North Atlantic. Pacific Deep Water, in contrast, carries less negative (i.e. more radiogenic)  $\epsilon_{Nd}$  values of  $\sim -4$  (e.g., Amakawa et al., 2009), due to the influence of weathering of younger volcanogenic material around the North Pacific. Modern CDW in the Southern Ocean is characterised by a relatively homogenous Nd isotope composition along the flow path of the ACC across all ocean basins and with depth ( $\epsilon_{Nd} = -8.3 \pm 1.5$ ;  $n = 158$ ) (Figs. 2A) (Lambelet et al., 2018 and references therein). In the western part of the Tasmanian Gateway along the ~140°E meridian, CDW exhibits  $\epsilon_{Nd}$  values of  $-8.6 \pm 0.4$  ( $n = 4$ ) around 2500–4300 m (Lambelet et al., 2018). In the eastern part of the gateway, in the Macquarie Ridge region, close to Site 278, CDW has  $\epsilon_{Nd}$  values of  $-9.0 \pm 0.2$  and  $-9.2 \pm 0.2$  between 3201 and 4183 m, respectively (Figs. 2A; S2) (Lambelet et al., 2018). Ross Sea Bottom Water exhibits a more radiogenic Nd isotope signature than CDW, probably acquired from Ross Sea shelf sediments and mixing with shelf waters ( $\epsilon_{Nd} = -6.5$  to  $-7.5$ ; Rickli et al., 2014; Basak et al., 2015) (Fig. 2B).

## 3. Materials and methods

### 3.1. Study sites, age models, and paleodepths

Our study focuses on the lower part of Hole 278 at DSDP Hole 278 (cores 34–26, 429–329 m below sea floor (mbsf)). Sediments from this interval consist of (i) siliceous nannofossil chalk (429–386 mbsf), and (ii) detrital and nannofossil-bearing radiolarian-diatom ooze, alternating with siliceous oozes (386–329 mbsf) (Kennett et al., 1975). A new age model for the studied sections of Site 278 has been established based on the integration of new magnetostratigraphic data with revised diatom, radiolarian and calcareous nannofossil biostratigraphy, calibrated to the Geological Time Scale (GPTS) 2012 (Gradstein et al., 2012) (Fig. 3; Supplementary Text; Tables S1–S4).

For DSDP Site 274, we focus on two distinct intervals (408.5–313.5 mbsf and 199.5–180.5 mbsf). Shipboard core descriptions report that sediments between 408.5 and 328 mbsf are composed of silty claystones

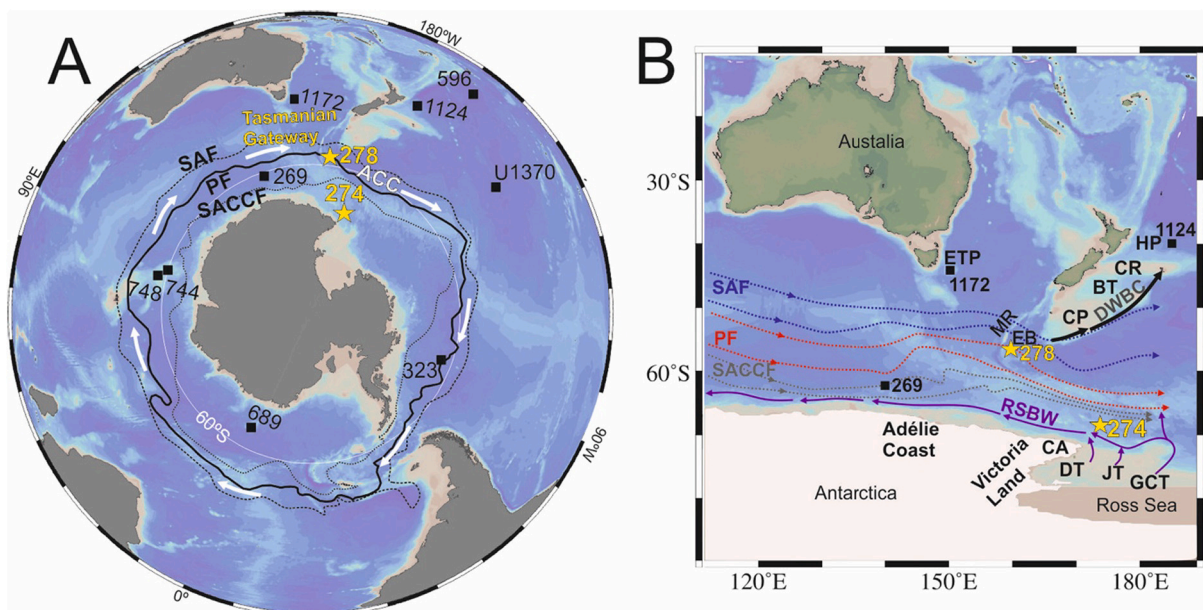


**Fig. 1.** Overview map of modern Southern Ocean configuration (Ocean Data View, (Schlitzer, 2016; version 4.79; <http://odv.awi.de>). **A:** Antarctic Circumpolar Current (ACC) frontal system, study sites (DSDP Sites 274 and 278) (yellow stars) and sites referred to in this study (black squares). SAF: Subantarctic front (black dashed line), PF: Polar front (black line), SACCF: Southern Antarctic Circumpolar Current front (black dotted line) adapted from Orsi et al. (1995). **B:** Major modern deep ocean water circulation paths across the Tasmanian Gateway adapted from Sokolov and Rintoul, (2007) and Gordon et al. (2009). The main transport of Circumpolar Deep Water along the ACC takes place around the PF and SAF, Ross Sea bottom water (RSBW) (purple) feeds Antarctic Bottom Water. Deep Western Boundary Current (DWBC) (black arrows), MR: Macquarie Ridge, EB: Emerald Basin, ETP: East Tasmanian Plateau, CP: Campbell Plateau, BT: Bounty Trough, CR: Chatham Rise, HP: Hikurangi Plateau, CA: Cape Adare, JT: Joides Trough, DB: Drygalski Trough, GCT: Glomar Challenger Trough. (For interpretation of the references to colour in this figure legend, the reader is referred to the web version of this article.)



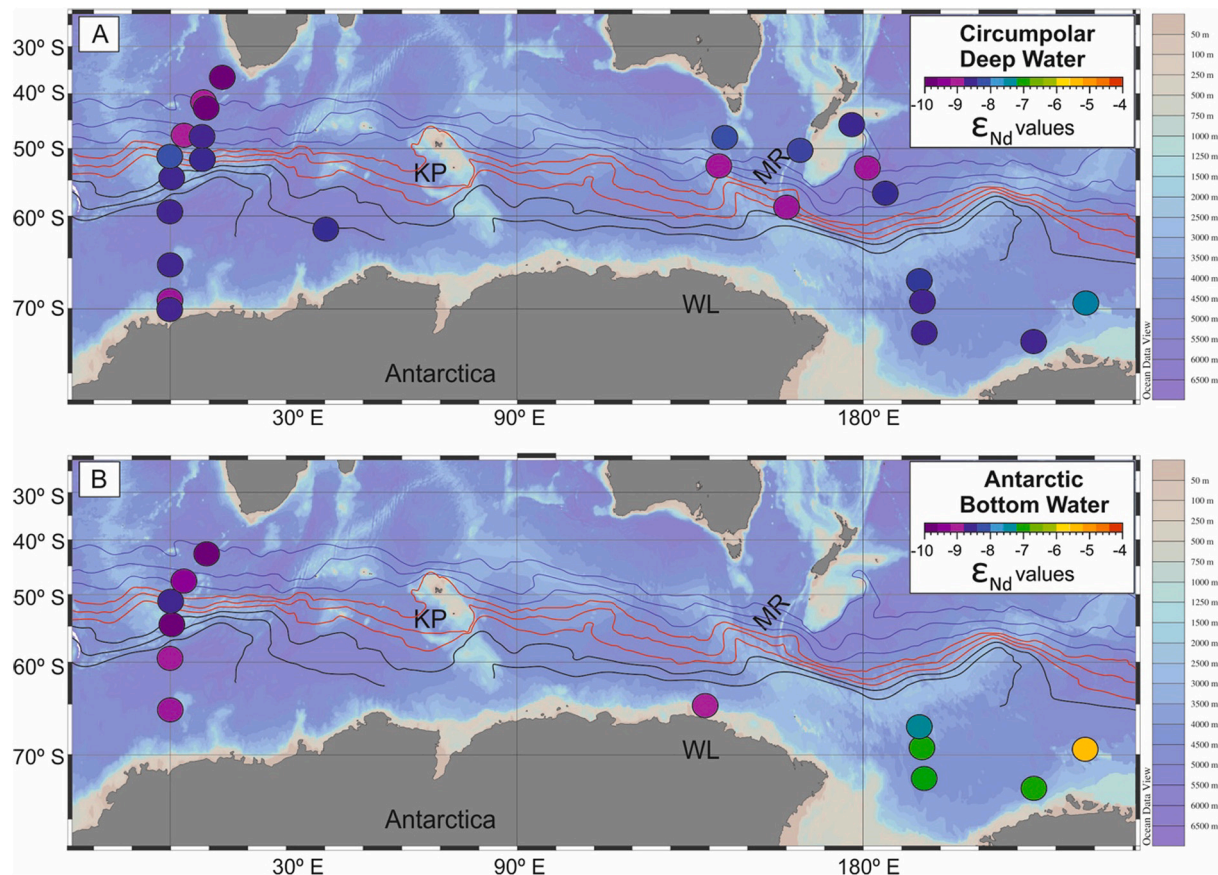


**Fig. 2.** Modern neodymium (Nd) isotope composition for deep and bottom waters in the Southern Ocean (between 0°E and 110°W). Figures are made with Ocean Data View (Schlitzer, 2016; version 4.79; <http://odv.awi.de>). (A): Nd isotope composition of Circumpolar Deep Water (CDW). (B): Nd isotope composition of Antarctic Bottom Water (AABW) (Stichel et al., 2012; Rickli et al., 2014; Garcia-Solsona et al., 2014; Basak et al., 2015; Lambelet et al., 2018; Amakawa et al., 2019). Antarctic Circumpolar Current (ACC) fronts (mean positions) adapted from Sokolov and Rintoul, 2007. SAF (blue), PF (red), SACCf (black), MR: Macquarie Ridge, WL: Wilkes Land, KP: Kerguelen Plateau. (For interpretation of the references to colour in this figure legend, the reader is referred to the web version of this article.)

with local presence of chert layers. Sediments between 323 and 180.5 mbsf consist of diatom-detrital silty clay and minor silty clay diatom ooze (Hayes and Frakes, 1975). Based on the initial age model, sediments between 408.5 and 180.5 mbsf are early to late Oligocene in age (Hayes and Frakes, 1975). New dinocyst constraints combined with new magnetostratigraphic data and revised diatom biostratigraphy (updated from Hayes and Frakes (1975)) calibrated to GPTS 2012 (Gradstein et al., 2012) provide an updated age model for the studied sediments at Site 274 from ~33.7 to 23.3 Ma (Fig. S4) (Hoem et al., 2021).

We reconstructed the paleoposition of Sites 278 and 274 using the G-plates geodynamic modeling (<http://www.gplates.org>; Müller et al., 2018), utilizing the plate circuit of Müller et al. (2016). Paleodepths for the sites were obtained from the paleo-bathymetry grids generated by the Earthbyte group (Scotese and Wright, 2018), incorporating the reconstructed paleolocation of the two sites (Fig. S5). Our reconstructions show that Site 278 migrated northwards from ~62.84°S (~30 Ma) to 61.4°S (~23 Ma); its paleodepth varied between 3500 and 4000 m throughout the Oligocene and early Miocene. Site 274 has migrated north from a position of ~70.22°S in the early Oligocene (~33 Ma) to ~69.57°S at the end of the Oligocene-Miocene transition (~23 Ma) and remained at ~2500–3000 m water depth throughout the Oligocene.

### 3.2. Neodymium isotope analyses

Fish teeth and bones (hereafter termed fish debris) were handpicked from the >63 μm sediment fractions isolated by wet sieving. A total number of 32 samples were selected for fish debris Nd isotope analyses

(20 samples from Site 278 and 12 samples from Site 274) (Table S5). All samples were treated with ultraclean 18 MΩ water (Milli-Q water) and methanol to remove debris from surfaces and cavities following Martin and Haley (2000) in the MAGIC laboratories at Imperial College London (see also Huck et al., 2017). Cleaned fish debris samples were subsequently transferred into cleaned microcentrifuge tubes and dissolved overnight in 50 μl of 2 M HCl. Dissolved fish debris were loaded on Biorad cation exchange resin (200–400 μm mesh) to separate the REEs from the sample matrix and Eichrom Ln-Spec resin (50–100 μm bead size) to separate Nd from the other REEs.

Furthermore, seven samples were selected (two from Site 278 and five from Site 274; Table S5) to determine the detrital Nd isotope composition in order to evaluate potential contribution of the detrital sediments to the porewaters or overlying bottom water signature. Samples were dried and gently homogenised using mortar and pestle. Approximately 500 mg of homogenised material was subjected to a carbonate leaching procedure to remove biogenic carbonate using 30 ml of 1.5% buffered acetic acid (modified from Biscaye (1965)). Due to the significant carbonate content of the samples from Site 278 (38 to 43%), approximately 1.5 g of dried sample and 70–75 ml of 1.5% buffered acetic acid were used. Exchangeable ions were subsequently removed using 10 ml 1 M MgCl<sub>2</sub> solution. In a third step, ferromanganese oxides and oxyhydroxides were removed using a weak reductive solution of 0.005 M Hydroxylamine Hydrochloride (NH<sub>2</sub>OH) 1.5% acetic acid and 0.03 M Na<sub>2</sub>-EDTA for one hour, followed by a stronger leaching step utilizing 0.05 M NH<sub>2</sub>OH for 17 h. 50 mg of leached and water washed detrital sediment was subsequently dried, weighted and digested on a hotplate using a mixture of 1 ml of concentrated HNO<sub>3</sub>, 0.8 ml HClO<sub>4</sub>

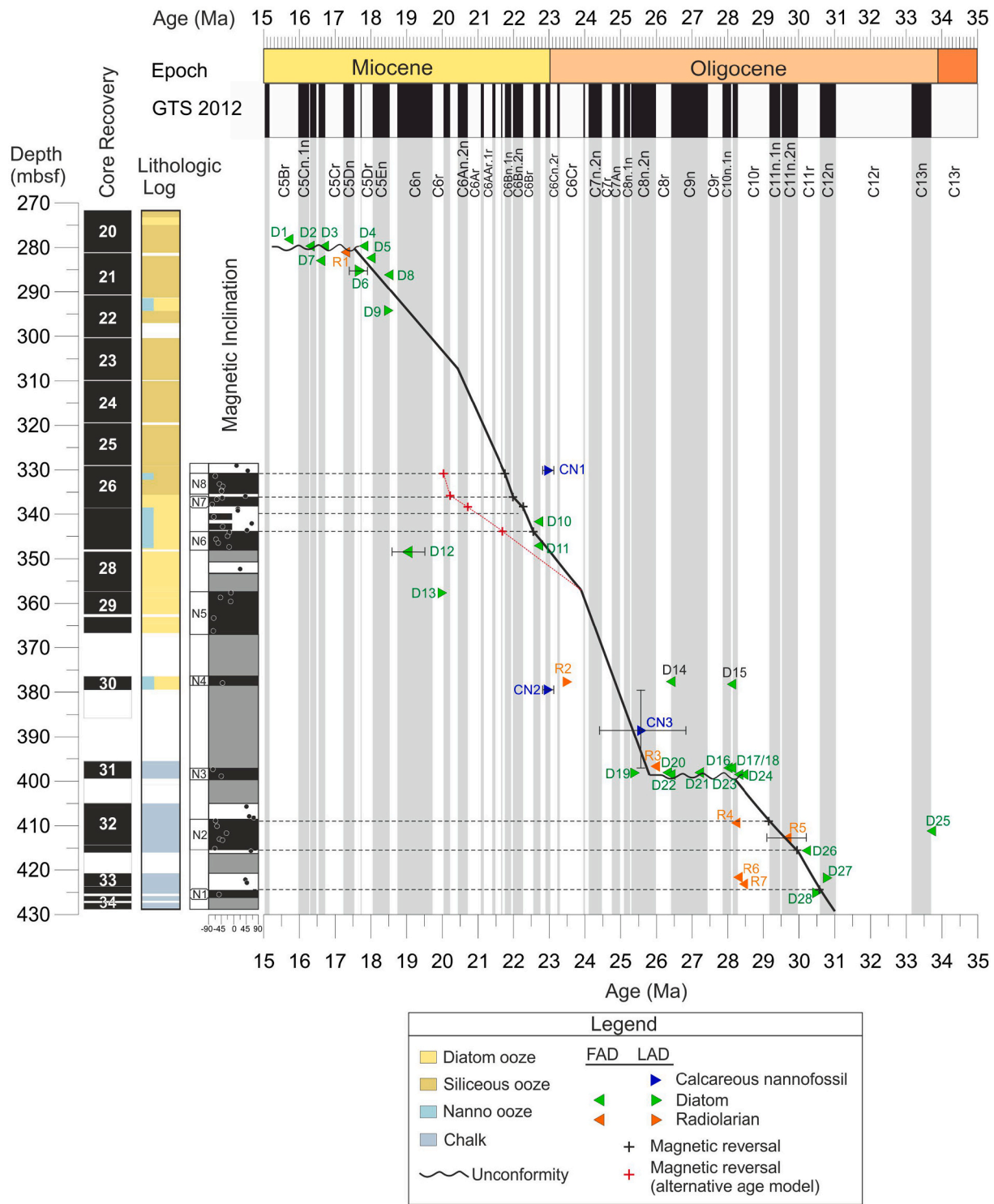


**Fig. 3.** Revised age-depth model for Site 278. Stratigraphy of Site 278, from left to right: depth in meters below sea floor (mbsf), core recovery, lithologic log based on initial shipboard sedimentological descriptions and local polarity based on inclination values. Grey vertical stripes mark the normal polarity zones of the geomagnetic polarity timescale (normal = black, reversed = white) (Gradstein et al., 2012). Black/red crosses = magnetostratigraphic constraints, green triangles = diatom biostratigraphic constraints, blue triangles = calcareous nannofossil biostratigraphic ranges, orange triangles = radiolarian biostratigraphic constraints. FAD = first appearance datum; LAD = last appearance datum. Horizontal error bars on biostratigraphic events indicate total age range for the given datum. Vertical error bars indicate the depth range for the given datum. Datum and biozone labels correspond to those in Tables: S1, S2, S3 and S4. The back line following the different constraints shows our preferred chronology, and in red a possible alternate. (For interpretation of the references to colour in this figure legend, the reader is referred to the web version of this article.)

and 2 ml HF. The detrital samples were processed using the same ion chromatography as the fish debris samples.

Neodymium isotope ratios of fish debris and detrital sediment samples were determined on a high-resolution Nu Plasma multiple collector inductively coupled plasma mass spectrometer (MC-ICP-MS) at Imperial College London, operated in static mode. Instrumental mass bias was corrected for using a  $^{146}\text{Nd}/^{144}\text{Nd}$  ratio of 0.7219. All reported  $^{143}\text{Nd}/^{144}\text{Nd}$  ratios are corrected to a nominal JNd<sub>i</sub> value of 0.512115 (Tanaka et al., 2000) using bracketing standards. JNd<sub>i</sub> standards were also used to monitor external reproducibility, and accuracy was evaluated by processing USGS BCR-2 rock standards alongside samples, which yielded average  $^{143}\text{Nd}/^{144}\text{Nd}$  ratios of  $0.512636 \pm 0.000008$  ( $n = 23$ ; 2 s.d.), in agreement with the published BCR-2  $^{143}\text{Nd}/^{144}\text{Nd}$  ratio of  $0.512638 \pm 0.000015$  (Weis et al., 2006) (Table S5).

### 3.3. Rare earth element analyses

To correct for the decay of  $^{147}\text{Sm}$  to  $^{144}\text{Nd}$  within the fish debris over time, we used the average Sm and Nd concentrations measured for two fish debris samples from Site 278 ( $^{147}\text{Sm}/^{144}\text{Nd}$  ratios of 0.1275 and 0.1256;  $^{147}\text{Sm}/^{144}\text{Nd}_{\text{average}} = 0.1266$ ) and three fish debris samples from Site 274 ( $^{147}\text{Sm}/^{144}\text{Nd}$  ratios of 0.1532, 0.1921, and 0.2662;  $^{147}\text{Sm}/^{144}\text{Nd}_{\text{average}} = 0.2038$ ). The range of Sm/Nd ratios reported here are consistent with values from Oligocene to Miocene fish debris material elsewhere (Huck et al., 2017; Wright et al., 2018; Evangelinos et al., 2020). Corrections for in situ decay of  $^{147}\text{Sm}$  amounted to 0.19 to 0.28  $\epsilon_{\text{Nd}}$  units for Site 278 and 0.02 to 0.14  $\epsilon_{\text{Nd}}$  units for Site 274; (t) denotes age-corrected samples (Table S5).

To investigate whether the Nd in the fish debris is of authigenic nature (i.e. seawater-derived), the full suite of REE concentrations were determined on one fish debris sample from Site 278 and three fish debris samples from Site 274 (Table S6). Rare earth element analysis was performed at the Open University using an Agilent Technologies 8800 Triple-Quad Inductively Coupled Plasma-Mass Spectrometer (ICP-MS). Analyses were standardized via a suite of seven synthetic multi-element standards made up with certified plasma standard solutions. An intermediate synthetic multi-element monitor standard, a fossil bone standard (Chavagnac et al., 2007) and a 2%  $\text{HNO}_3$  blank were run every 5th sample to monitor instrument drift and precision. Precision was generally better than  $\pm 2\%$  (1 s.d.). Both oxide interferences ( $\text{CeO}^+/\text{CeO}^-$ ) ( $<0.5\%$ ) and doubly charged species ( $\text{Ce}^{++}/\text{Ce}^+$ ) ( $<1.2\%$ ) were kept low. All REE data were normalised to Post Archean Shale (PAAS) concentrations (Taylor and McLennan, 1985).

## 4. Results

### 4.1. Age model DSDP Site 278

An age-depth model for the Oligocene and lower Miocene intervals of DSDP Site 278 is developed from the integration of new magnetostratigraphic data, calcareous nannofossil, marine diatom, and radiolarian biostratigraphy, calibrated using the Geological Time Scale (GPTS) 2012 (Gradstein et al., 2012) (Figs. 3; Supplementary Text; Tables S1–S4). We also present an alternate age model that fit with the constraints of the data (for details see supplementary material). The stratigraphic section cored at Site 278 from the bottom of the sedimentary section in core 34 at  $\sim 429$  mbsf up to sample 278-21R-1, 50 cm at  $\sim 282$  mbsf spans the time interval from  $\sim 31$  to 17.7 Ma, with one unconformity noted between samples 278-31R-3, 35 cm and 278-31R-2, 139 cm (398.85–399.89 mbsf), which removed a  $\sim 2.4$  m.y. time interval from 28.2 to 25.8 Ma. The top of this interval is bounded by an unconformity between samples 278-21R-1, 50 cm and 278-20R-6, 50 cm (281.5 mbsf), which removed the time interval 17.6 to 15.5 Ma (Fig. 3). Studied sediments (cores 34R-26R) are dated between  $\sim 31$  and 21.7 Ma, similar to the initial shipboard ages (Fig. 3), suggesting upper Oligocene to lower Miocene sediments (Kennett et al., 1975).

### 4.2. Fish debris Nd isotope compositions

Fish debris Nd isotope data from Site 278 show little variability, ranging from  $\epsilon_{\text{Nd}(t)} = -6.0 \pm 0.2$  to  $6.7 \pm 0.2$  from the early Oligocene to the early Miocene ( $\sim 30.9$ – $21.8$  Ma) (Fig. 4; Fig. S6A; Table S5). The average  $\epsilon_{\text{Nd}(t)}$  throughout the record is  $-6.4 \pm 0.2$  ( $n = 20$ ). In contrast, fish debris Nd isotope data from Site 274 show more variability, and reach to maximum values of  $-3.1 \pm 0.3$  at 33.5 Ma and  $-3.7 \pm 0.3$  at 23.8 Ma to relative minima of  $-5.0 \pm 0.1$ , at  $\sim 33.2$ – $29.7$  Ma,  $-6.2 \pm 0$  at  $\sim 29$  Ma,  $-7.3 \pm 0.3$  and  $-6.8 \pm 0.2$  at  $\sim 24.3$  and 24.0 Ma, respectively (Fig. 4; Fig. S6B; Table S5). The late Oligocene time period features a pronounced excursion to more radiogenic  $\epsilon_{\text{Nd}(t)}$  values by  $\sim 3$  epsilon units between 24.0 and 23.8 Ma.

### 4.3. Bulk sediment Nd isotope compositions

The detrital samples at Site 278 exhibit  $\epsilon_{\text{Nd}(t)}$  values of  $-10.4 \pm 0.3$  ( $\sim 30.5$  Ma) and  $-7.9 \pm 0.3$  ( $\sim 21.8$  Ma), respectively (Fig. 4; Fig. S6A; Table S5). Lower Oligocene detrital sediment Nd isotope compositions from Site 274 exhibit  $\epsilon_{\text{Nd}(t)}$  values of  $-4.2 \pm 0.3$  ( $\sim 33.5$  Ma),  $-7.6 \pm 0.3$  ( $\sim 33.2$  Ma) and  $-8.5 \pm 0.3$  ( $\sim 29$  Ma). Two additional late Oligocene detrital sediment samples yielded  $\epsilon_{\text{Nd}(t)}$  values of  $-10.3 \pm 0.3$  and  $-8.5 \pm 0.3$  at  $\sim 24.0$  Ma and 23.8 Ma, respectively (Fig. 4; Fig. S6B; Table S5).

### 4.4. Fish debris REE patterns

Five fish debris samples from Site 278 and Site 274 yielded middle-REE enriched patterns (Fig. 5; Table S6). Only one sample from section 278-33R-6 showed a negative Ce anomaly, which together with the middle-REE enriched patterns represent a diagnostic feature of seawater-derived Nd in fish teeth samples (Scher et al., 2011).

## 5. Discussion

### 5.1. Reliability of Nd isotopes from Sites 278 and 274

Results of Oligocene to Miocene-aged fish debris samples at Site 278 (paleodepth: 3500–4000 m) are more radiogenic (less negative) in their Nd isotope composition ( $\epsilon_{\text{Nd}(t)} = -6.0$  to  $-6.7$ ) than modern CDW in the south Emerald Basin ( $\epsilon_{\text{Nd}} = \sim -9$ ) at  $\sim 3200$ – $4200$  m water depth (Lambelet et al., 2018). Results for Site 274 ( $\epsilon_{\text{Nd}(t)} = -3.1$  to  $-7.3$ ) show generally more radiogenic values compared to ambient RSBW ( $\epsilon_{\text{Nd}} = -6.5$  to  $-7.5$ ; Rickli et al., 2014; Basak et al., 2015) (Fig. 4). The first question to address is if the fish debris record a purely authigenic signal.

Site 278 is located near the Macquarie Ridge, a relict volcanic mid-ocean ridge, characterised by basalts and peridotites with an  $\epsilon_{\text{Nd}}$  value of  $+7$  to  $+11$  (Dijkstra et al., 2009; Conway et al., 2012). Interaction of volcanic sediments and/or hydrothermal products with ambient seawater could have altered the  $\epsilon_{\text{Nd}}$  values at Site 278 towards more radiogenic values. However, hydrothermal activity has been shown to be a sink rather than a source of Nd near ridges (Stichel et al., 2018). Moreover, fish teeth records from the Kerguelen Plateau show no changes in their Nd isotopic composition associated with the local volcanic activity during the timing of the northern Kerguelen Plateau emplacement (Wright et al., 2018). Volcanic glass and rock fragments have been reported from close to the base of siliceous nannofossil chalk at Site 278 (Kennett et al., 1975) ( $\sim 31$ – $28.2$  Ma, based on our new age model). However, the lack of any significant variability in our fish debris Nd record makes it difficult to reconcile any major volcanic contribution to the porewater and hence to the fish debris Nd isotope signature (Figs. 4; S7A).

To further evaluate the potential interaction between detrital sediments and pore water/seawater Nd isotope composition, we can use the results from two detrital sediment samples from the siliceous chalk unit (section 33R-6) and from the nannofossil-bearing diatom ooze unit (section 26R-2) at Site 278. The detrital samples exhibit  $\epsilon_{\text{Nd}(t)}$  values of



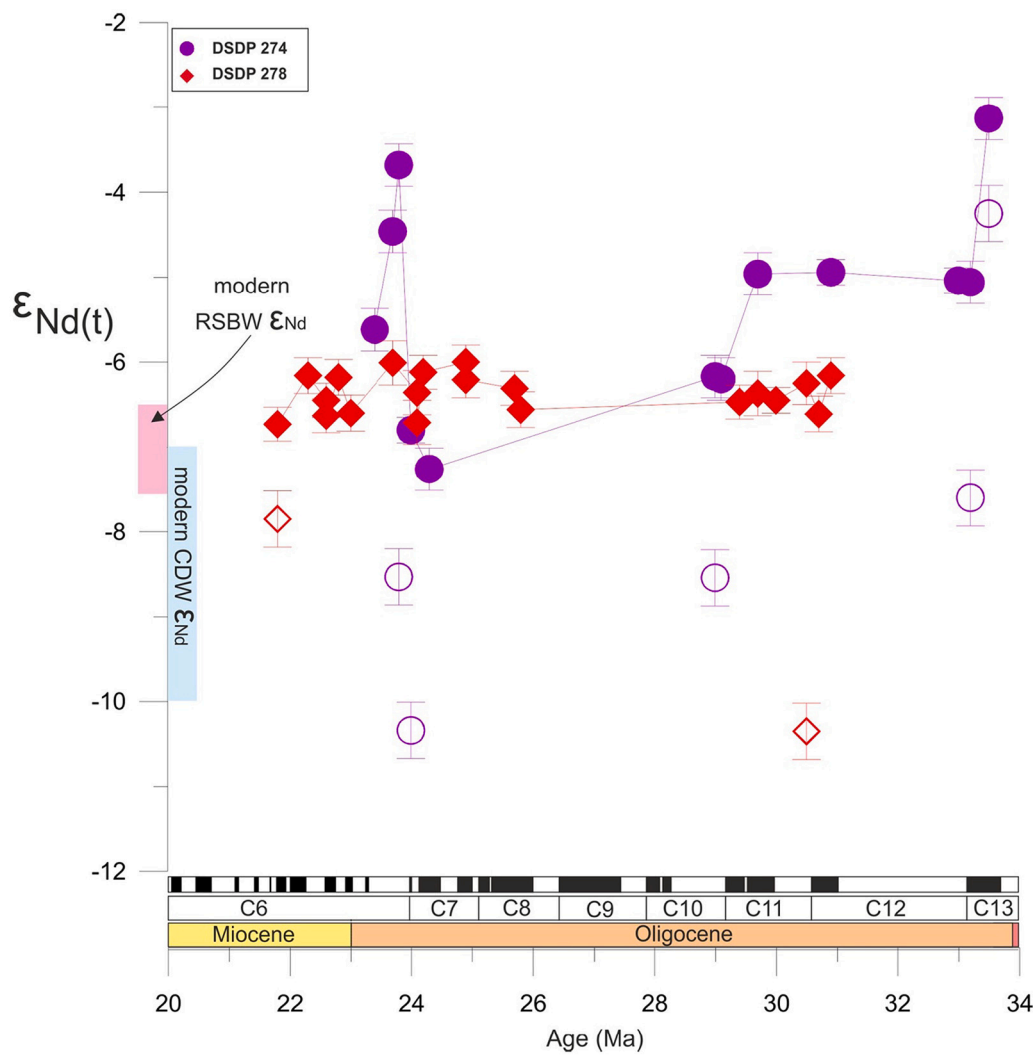


**Fig. 4.** Fish debris  $\epsilon_{Nd(t)}$  records generated in this study from DSDP Sites 274 (purple circles) and 278 (red diamonds). Detrital sediment  $\epsilon_{Nd(t)}$  values from DSDP Sites 274 (purple open circles) and 278 (red open diamonds). Present-day Ross Sea Bottom Water (RSBW)  $\epsilon_{Nd}$  endmember ranges shown in magenta (Rickli et al., 2014; Basak et al., 2015). Present-day Circumpolar Deep Water (CDW)  $\epsilon_{Nd}$  endmember ranges shown in blue (Lambelet et al., 2018 and references therein). (For interpretation of the references to colour in this figure legend, the reader is referred to the web version of this article.)

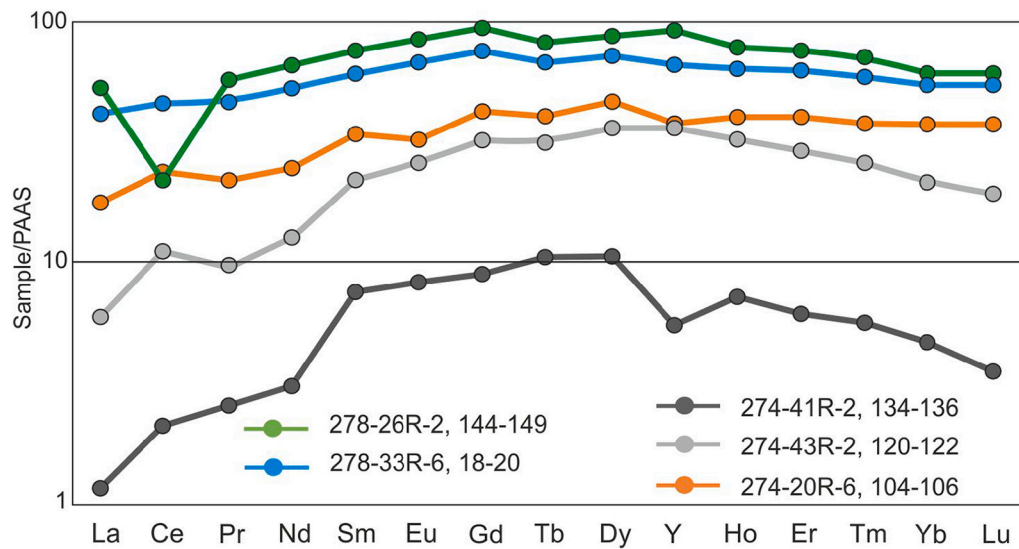


**Fig. 5.** Rare earth element (REE) patterns normalised to Post Archean Shale (PAAS) concentrations (Taylor and McLennan, 1985) for DSDP Sites 278 and 274.

$-10.4 \pm 0.3$  and  $-7.9 \pm 0.3$ , respectively (Fig. 4; Table S5), within the range of terrigenous inputs from Paleozoic granites and metasedimentary rocks ( $\epsilon_{Nd(t)} = -4.9$  to  $-13.9$ ) of the South Island, New Zealand (Pickett and Wasserburg, 1989). This observation is in line with the general deep water flow in the area, suggesting that terrigenous sediments in the Southern Emerald Basin are predominantly derived from the erosion of the New Zealand's Southern Alps via the Solander Channel (Carter and McCave, 1997). Importantly, the measured detrital sediment composition is more unradiogenic (i.e. more negative  $\epsilon_{Nd}$  values) than the almost contemporaneous fish debris signatures and hence cannot be responsible for the observed more radiogenic values. In addition, REE patterns from a fish debris sample from section 33R-6 (~30.5 Ma) exhibit a pattern enriched in middle-REEs and a prominent negative cerium (Ce) anomaly, which represent diagnostic features of uncontaminated seawater origin in the fish debris (Fig. 5; Table S6) (Scher et al., 2011; Huck et al., 2016, 2017). The fish debris sample from section 26R-2 (21.8 Ma) exhibit also a typical middle-REEs enriched pattern but records a slightly positive Ce anomaly (Fig. 5). Positive Ce anomalies in fish debris have been linked to anoxic seawater and/or pore water conditions, resulting in remobilization of REEs from authigenic or organic matter coatings (Elderfield and Pagett, 1986; Freslon

et al., 2014; Huck et al., 2016). High biogenic productivity at Site 278 associated with proto-polar front upwelling processes (Kennett et al., 1975) may have led to anoxic conditions at the seafloor.

Similar to Site 278, bulk sediment results from Site 274 exhibit a less radiogenic (i.e. lower) Nd isotope fingerprint than fish debris when comparing results for the same samples and samples taken very close to each other. The difference in  $\epsilon_{Nd(t)}$  for three pairs of fish debris-detrital sediment samples analyzed is  $-4.9$ ,  $-3.5$  and  $-2.4$   $\epsilon_{Nd}$  units, while adjacent samples show differences in  $\epsilon_{Nd(t)}$  of  $-2.5$  and  $-1.1$  (Figs. 4; S7B; Table S5). This pronounced difference between the  $\epsilon_{Nd(t)}$  values of the fish debris and the detrital sediment samples at Site 274 strongly supports the absence of significant exchange between the detrital sediments and the fish debris. Overall, the more radiogenic  $\epsilon_{Nd(t)}$  values of the fish debris, compared to the more unradiogenic  $\epsilon_{Nd(t)}$  values of the detrital samples, argues against a contribution of Nd from the detrital sediments.

Furthermore, REE patterns of three fish debris samples at Site 274 yielded middle-REE bulge patterns, including a slightly positive Ce anomaly (Figs. 5; Table S6). The close proximity of Site 274 to the Antarctic continental margin and the high biogenic fraction in the sediment (Hayes and Frakes, 1975) may have caused the observed

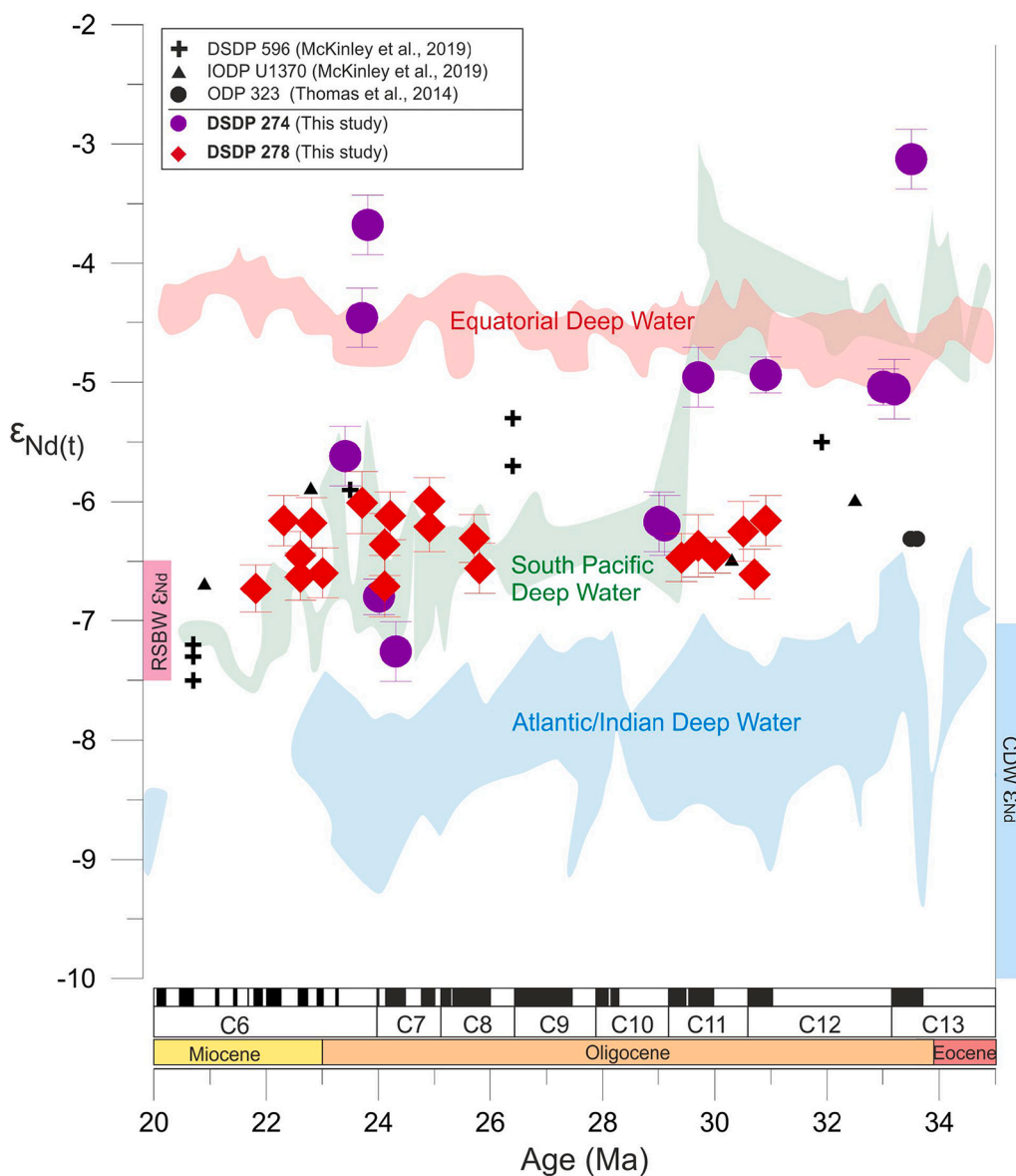


Fig. 6. Comparison of fish debris  $\epsilon_{Nd}$  records generated in this study from DSDP Sites 274 and 278 with those derived from sites along the proto-CDW path in the Atlantic, Indian and Pacific sectors of the Southern Ocean. Atlantic/Indian Ocean locations include ODP Site 689 (Maud Rise; Scher and Martin, 2004), ODP Sites 748 and 744 (Kerguelen Plateau; Wright et al., 2018), and DSDP Site 269 (off Adélie Coast; Evangelinos et al., 2020) (light blue shading). ODP Site 1124 (Hikurangi Plateau) and ODP Site 1172 (East Tasmanian Plateau; Scher et al., 2015) are combined in the green shading. Pacific Equatorial Age Transect (PEAT) Nd isotope results from the Equatorial Pacific are based on IODP Sites U1331, U1332, U1333, U1334, and U1335 (Scher, 2014) (red shading). The only data shown as individual symbols other than our new results are South Pacific DSDP Site 596, IODP Site U1370 (McKinley et al., 2019) and ODP Site 323 (Thomas et al., 2014). Blue shaded ranges refer to the present-day Nd signature of the CDW and magenta shaded rangers refer to the present-day Nd isotopic composition of the RSBW (Rickli et al., 2014; Basak et al., 2015; Lambelet et al., 2018 and references therein). (For interpretation of the references to colour in this figure legend, the reader is referred to the web version of this article.)



positive Ce anomaly resulting from increased weathering inputs and/or remobilized REEs from authigenic or organic matter coatings due to anoxic conditions in the pore waters (Elderfield and Pagett, 1986; Frezslon et al., 2014; Huck et al., 2016). Further work is required to fully understand the positive Ce anomaly in our fish debris samples. Nevertheless, REE patterns from Site 278 and 274 are similar to REE patterns from Eocene-Oligocene fish debris records from around the Tasmanian Gateway, which have been interpreted to preserve a predominantly seawater signature, despite positive Ce anomalies (Huck et al., 2016, 2017). We therefore suggest an authigenic nature of the fish debris record from Sites 278 and 274 and use our new data to explore the chemical fingerprint of proto-CDW and RSBW across the Tasmanian Gateway, and its implications for the ACC evolution.

### 5.2. Early Oligocene epoch (33–30 Ma): Prior to the inferred onset of the ACC throughflow via the Tasmanian Gateway

Neodymium isotope values from our deeper Site 278 (paleodepth: ~4000 m) between 31 and 30 Ma, indicate that the southern Emerald Basin was bathed by an unradiogenic deep water mass ( $\epsilon_{\text{Nd}(t)} = \sim -6.4$ ) (Figs. 4; 6). These values converge with published Nd isotope records from the deep South Pacific (Site U1370, paleodepth ~5000 m, Site 596 paleodepth ~5000 m and Site 323, paleodepth ~4000 m;  $\epsilon_{\text{Nd}(t)} = \sim -6.3$ ) (Thomas et al., 2014; McKinley et al., 2019), suggesting that abyssal sites in the South Pacific were likely influenced by a common deep/bottom water mass, such as South Pacific Deep Water (SPDW) (Fig. 6). Temporal and spatial Nd isotope patterns and modeling results show that SPDW was a prominent and persistent water mass of the deep ( $\geq 3500$  m) South Pacific (between at least ~30°S–63°S) from 70 to 20 Ma, characterised by  $\epsilon_{\text{Nd}(t)}$  of  $\sim -6$  (Thomas et al., 2014; McKinley et al., 2019; Sarkar et al., 2019). We therefore suggest that Site 278 (paleodepth: ~63°S) was bathed by SPDW between 33 and 30 Ma.

Neodymium isotope records consistent with model results indicate bimodal mode of deep ocean circulation in the Pacific Ocean from ~70 to 25 Ma (Scher, 2014; Thomas et al., 2014; Scher et al., 2015; Huck et al., 2017; McKinley et al., 2019; Sarkar et al., 2019). Convection of SPDW occurred in the South Pacific (likely in the Ross Sea region), while North Pacific Deep Water (NPDW) formation occurred in the North Pacific. Our  $\epsilon_{\text{Nd}(t)}$  values from Site 274, located proximal to the Ross Sea, however, range from  $-3.1$  to  $-5$  between 33.5 and 29.7 Ma and albeit of low resolution are more radiogenic (less negative), compared to both the present-day RSBW Nd isotopic composition ( $\epsilon_{\text{Nd}} = -6.4$  to  $-7.5$ ; Rickli et al., 2014; Basak et al., 2015) and the deep record from Site 278 (Figs. 4; 6). The average  $\epsilon_{\text{Nd}(t)}$  value of  $\sim -4.6$  for the early Oligocene (~33.5–29.7 Ma) at Site 274 (paleodepth: ~2500–3000 m) overlaps with published data from the East Tasman Plateau (Site 1172; average  $\epsilon_{\text{Nd}(t)} = \sim -4.2$  paleodepth: ~2400 m) and Hikurangi Plateau (Site 1124; average  $\epsilon_{\text{Nd}(t)} = \sim -4.6$ ; paleodepth: ~3000 m) (Scher et al., 2015; Sarkar et al., 2019) (Fig. 6). Similarities in Nd isotope values and paleodepths between the Antarctic margin record from Site 274 and the published records for the northern parts of the Tasmanian Gateway (Sites 1172 and 1124; Scher et al., 2015), suggest that these sites may have been influenced by a common water mass, occupying water depths between ~2500 and 3000 m. This more radiogenic signature is akin to northern sources Equatorial Pacific Deep Water (Fig. 6) (Scher, 2014), which originated in the deep Equatorial Pacific, where NPDW and SPDW mixed (Thomas et al., 2014). Neodymium isotope data from Sites 1172 and 1124 suggest that Equatorial Pacific water was present at 2500–3000 m, reaching at least to southern latitudes of 60°S–65°S between 36 and 30 Ma (Scher et al., 2015; Sarkar et al., 2019). We here suggest that water from a northern source with a more Equatorial Pacific-like Nd isotope signature reached to the Adare Basin (Site 274, ~70°S) between 33 and 30 Ma.

Our results point to the presence of two distinct deep water masses in the late Eocene/early Oligocene South Pacific: one occupying depths between ~2500 and 3000 m with Nd composition ( $\epsilon_{\text{Nd}(t)} = \sim -3$  to  $-5$ )

and a second deep/bottom water mass ( $> 3000$  m) with more unradiogenic Nd composition ( $\epsilon_{\text{Nd}(t)} = \sim -6$ ) (Fig. 6).

### 5.3. Early Oligocene to early Miocene epoch (30–22 Ma): After the inferred onset of the ACC throughflow via the Tasmanian Gateway

Neodymium isotope values at Site 274 show a shift towards less radiogenic values ( $\epsilon_{\text{Nd}(t)} = -6.2 \pm 0.3$ ) between 29.7 and 29.1 Ma. Slightly less radiogenic  $\epsilon_{\text{Nd}(t)}$  values are observed around 24.3 Ma and 24.0 Ma ( $-7.3 \pm 0.25$  and  $-6.8 \pm 0.15$ , respectively) (Figs. 4; 6), resembling modern RSBW values ( $\epsilon_{\text{Nd}} = -6.4$  to  $-7.5$ ; Rickli et al., 2014; Basak et al., 2015). The shift between 29.7 and 29.1 Ma at Site 274 coincides with the shift observed in the two Nd isotope records from the East Tasman Plateau (Site 1172  $\epsilon_{\text{Nd}(t)} = -4.8$  to  $-6.8$ ) and the Hikurangi Plateau (Site 1124  $\epsilon_{\text{Nd}(t)} = -5.6$  to  $-6.2$ ) between 29.6 and 29 Ma, respectively (Scher et al., 2015) (Fig. 6). This latter shift has been linked to the northward migration and alignment of the Tasmanian Gateway with the westerly winds (Scher et al., 2015). The change in the  $\epsilon_{\text{Nd}(t)}$  values at Site 274 between 29.7 and 29.1 Ma does not coincide with any significant known change in the Antarctic ice sheet that would have influenced the sediment input around the Ross Sea. Instead, given that Site 274 was located south of the proto-PF during this period (Nelson and Cooke, 2001; Scher et al., 2015), we posit that the shift to more unradiogenic Nd contribution is probably due to the onset of proto-CDW upwelling reaching the Adare Basin and Site 274.

Site 278, on the other hand, was located close to the proto-PF and proto-SAF between 30 Ma and 22 Ma and thus in the main pathway of the proto-ACC and proto-CDW (Nelson and Cooke, 2001), explaining its invariant Nd isotope fingerprint (average  $\epsilon_{\text{Nd}(t)} = -6.4$ ) throughout the early Oligocene to early Miocene (29.7–22 Ma) (Figs. 4; 6). These values are matched by the two published Nd isotope records (Sites 1172 and 1124;  $\epsilon_{\text{Nd}(t)} \sim -6.5$ ) from the eastern side of Tasmanian Gateway after the onset of ACC influence at this northern location (Scher et al., 2015) (Fig. 5). All three records show more radiogenic Nd isotope compositions than modern CDW in the Emerald Basin ( $\epsilon_{\text{Nd}} = -9$ ; Lambelet et al., 2018) (Figs. 2A; S2). They furthermore differ from records to the west of the Tasmanian Gateway. Throughout the Oligocene (30–23 Ma) Nd isotope records along the proto-PF in the South Atlantic and the South Indian Ocean are characterised by proto-CDW with a Nd isotope composition between  $\sim -7$  and  $-9$  (Site 689: Scher and Martin, 2004; Site 748 and 744: Wright et al., 2018; Site 269: Evangelinos et al., 2020) (Figs. 6; 7). Such values are similar to modern CDW ( $\epsilon_{\text{Nd}} = -8.3 \pm 1.5$ ,  $n = 158$ ) (Lambelet et al., 2018) (Fig. 6).

Comparison between our new and previously published data along the proto-ACC pathway around the Tasmanian Gateway therefore reveals a provincially in seawater Nd isotopes with more radiogenic proto-CDW ( $\epsilon_{\text{Nd}(t)} = -6$  to  $-7.5$ ) on the Pacific side of the Tasmanian Gateway, and less radiogenic proto-CDW ( $\epsilon_{\text{Nd}(t)} = -7$  to  $-9$ ) in the Indian and Atlantic sectors of the Southern Ocean (Figs. 6; 7). This observation implies an absence of a homogenous deep water mass across the Tasmanian Gateway during the Oligocene and early Miocene, and suggests a more complex evolution of the deep ocean circulation across the gateway than previously assumed.

We propose that the provincially in water mass signatures across the gateway was due to a less deep reaching and probably also weaker proto-ACC flow during the Oligocene to early Miocene (Fig. 7). A shallower and weaker ACC flow entering the South Pacific would have increased the amount of time that Pacific deep water could have mixed with the proto-CDW, allowing for acquisition of a more radiogenic isotopic composition of proto-CDW. These inferences are consistent with numerical simulations showing limited throughflow of the proto-ACC due to Australasian paleogeography during the Oligocene (Hill et al., 2013) and weaker global overturning circulation due to weaker westerly winds from the early to mid-Miocene (Herold et al., 2012).

Recently collected sedimentological data, microfossil assemblages and past reconstructions of sea surface temperatures from the Antarctic-

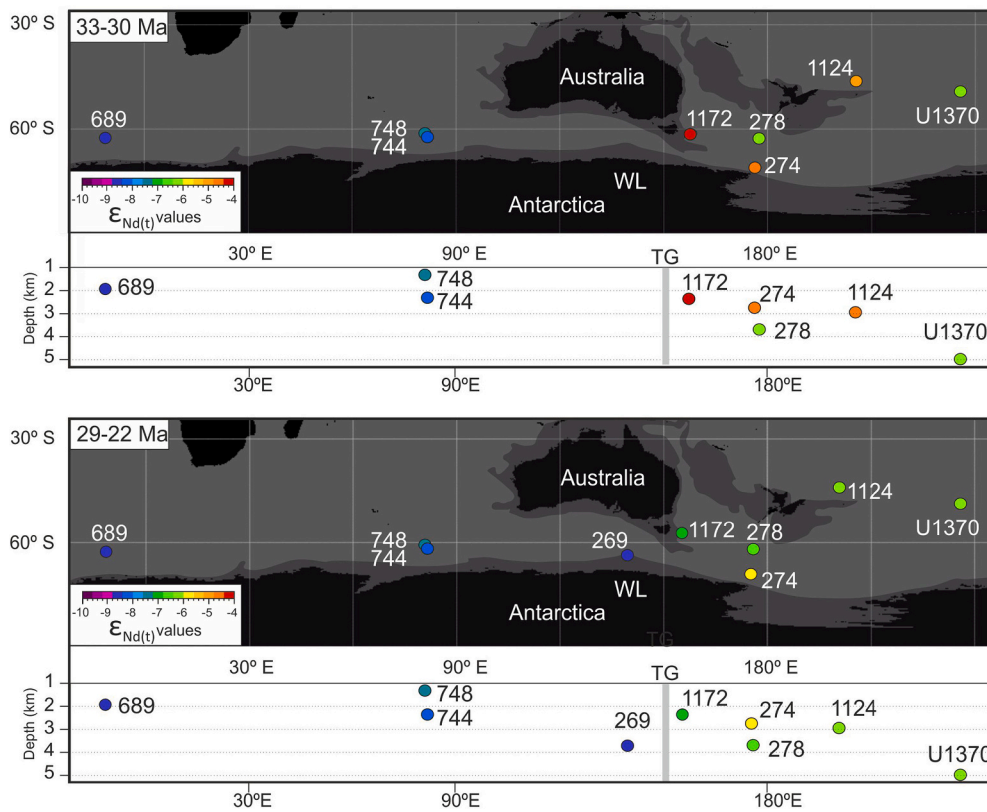


**Fig. 7.** Map of neodymium (Nd) isotopic data discussed in the main text plotted against paleo-latitude and longitude (upper panels) and paleo-depth (lower panels) from 33 Ma to 30 Ma and from 29 to 22 Ma. Plate tectonic reconstructions and paleo-location of study Sites 278 and 274, and other sites discussed in the main text were adapted from G-plates, based on the global plate motion model from Müller et al. (2016). Continent with present-day coastlines (black), grey boundary around continents shows areas of non-oceanic crust (e.g. continental shelves). Circles represent site locations and are coloured based on their average  $\epsilon_{Nd(t)}$  values for each period considered. Grey band indicates the position of the Tasmanian Gateway (TG).

Australian Basin and around the Tasmanian Gateway, also infer a weaker proto-ACC frontal system, characterised by intrusions of warm waters from northern latitudes from the Oligocene to the middle Miocene, weak latitudinal paleotemperature gradients and absence of strong sea ice seasonality (34–11 Ma) (Bijl et al., 2018; Hartman et al., 2018; Salabarnada et al., 2018; Sangiorgi et al., 2018; Evangelinos et al., 2020; Hoem et al., 2021). The question remains when the modern-like ACC was established. Our data suggest that this occurred during the Neogene, but future work is necessary to address the timing of its establishment and the wider implications of a weaker Oligocene to Miocene ACC.

#### 5.4. Evidence of a glacial weathering event during the latest Oligocene (~24 Ma)

The most pronounced  $\epsilon_{Nd}$  excursion observed at Site 274 (from  $-6.8 \pm 0.3$  to  $-3.7 \pm 0.3$ ) between 24.0 and 23.8 Ma is a peculiar feature of our new record and may reflect a local change in seawater composition (Figs. 4; 6). Although only represented by a single data point, another radiogenic isotope excursion is hinted at  $\sim 33.5$  Ma ( $\epsilon_{Nd(t)} = -3.1 \pm 0.3$ ; Figs. 4; 6). Considering the relatively invariant Nd isotope compositions of Oligocene Pacific deep water (Scher, 2014; McKinley et al., 2019) and proto-CDW (this study; Wright et al., 2018; Evangelinos et al., 2020) during the Oligocene, we consider two potential causes for the radiogenic excursion at Site 274: (i) increased boundary exchange/volcanic activity, and (ii) pulses in Antarctic ice advance leading to increased weathering inputs to local seawater.

Volcanic activity and deposition of material from the McMurdo volcanic group ( $\epsilon_{Nd} > 0$ ; see references in Cook et al., 2013) have been reported to occur predominantly after 24 Ma (Roberts et al., 2013). In addition, there is little physical evidence of volcanic contributions to the sediments at Site 274 (Hayes and Frakes, 1975), an observation that is confirmed by our measured detrital sediment  $\epsilon_{Nd(t)}$  values of  $-8.5 \pm 0.3$  (Fig. 4). Furthermore, REE patterns indicate that fish debris

predominantly preserve a seawater signature at 23.8 Ma (Fig. 5). We therefore exclude the possibility of boundary exchange/volcanic activity as a cause for the positive Nd isotope excursion.

A more promising connection can be made with the timing of a major expansion of ice from Antarctica. The Eocene-Oligocene transition is well documented as a major ice advance on Antarctica (e.g., Zachos et al., 1992; Galeotti et al., 2016). A seawater expression of weathering inputs from this ice expansion has been documented in the Prydz Bay area, where late Eocene and Eocene Oligocene Transition (EOT) fish teeth show a shift in seawater composition consistent with increased Antarctic weathering inputs (Scher et al., 2011; Bohaty et al., 2012; Wright et al., 2018). Even though only documented by a single data point, the very radiogenic  $\epsilon_{Nd(t)}$  value of  $-3.1 \pm 0.3$ , our Site 274 exhibits the most extreme Nd isotope signature  $\sim 33.5$  Ma (Figs. 4; 6). A shift towards more radiogenic values may indicate erosion and delivery of more radiogenic material exposed upstream in the Transantarctic Mountains, such as basalts and sills of the Ferrar Large Igneous Province ( $\epsilon_{Nd}$ :  $-3.5$  to  $-6.9$ ; see Cook et al., 2013 for a summary) or rocks like the Granite Harbour Intrusives in the Gabbro Hills ( $\epsilon_{Nd} = \sim -2.3 \pm 1.6$ ,  $n = 4$ ; Borg et al., 1990).

Interestingly, our data clearly define a second major seawater Nd isotope excursion between 24.0 and 23.8 Ma, which appears to be closely associated with one of the most significant climate transitions since the EOT resulting in a major Antarctic ice sheet expansion ( $\sim 24.5$ –24 Ma; Levy et al., 2019). Kulhanek et al. (2019) described the first occurrence of ice proximal glaciomarine sediments from DSDP Site 270 on the shelf of the Ross Sea at this time. In addition unconformities are observed at another Ross Sea drill site proximal to the Transantarctic Mountains (CRP-2/2A; Naish et al., 2008), and in seismic data (Sorlien et al., 2007), which are consistent with the first major expansion of marine ice sheets across the Ross Sea continental shelf (see also Levy et al., 2019). We consider it very likely that large changes in the Antarctic cryosphere, i.e. large ice advance in this case, would have changed significantly the erosional input from Antarctica to the Ross Sea margin,

and hence would have imprinted a radiogenic Nd isotope signal in local seawater.

## 6. Conclusions

New Oligocene to Miocene seawater Nd isotope data from Site 274 in the Adare Basin, Ross Sea, reveal two major shifts in seawater chemistry in response to major steps in Antarctic ice sheet expansion at the Eocene/Oligocene boundary (33.7 Ma) and between ~24.5 and 24.0 Ma. In contrast, Site 278 in the southern Emerald Basin shows an invariant Nd isotopic composition ( $\epsilon_{\text{Nd}(t)} = -6.0$  to  $-6.7$ ) throughout the Oligocene and early Miocene (31–22 Ma). Comparison with previously published data suggests the presence of two deep water masses in the South Pacific prior to the inferred onset of the ACC (34–30 Ma), one occupying depths between ~2500 and 3000 m with Nd composition  $\epsilon_{\text{Nd}(t)} = -3$  to  $-5$  and a deep/bottom water mass (>3000 m) with more unradiogenic Nd composition ( $\epsilon_{\text{Nd}(t)} \sim -6$ ). Following the onset of the ACC and the opening of the Tasman Gateway (30–22 Ma), the seawater Nd isotope record at Site 278, remained more radiogenic than the proto-CDW in the South Atlantic and Indian Ocean. We attribute the provinciality in the Nd isotope composition of deep waters across the Tasmanian Gateway to a weaker, less deep reaching ACC (proto-ACC) than today. Our finding implies that the modern strong and deep-reaching ACC, which creates a near homogenous Southern Ocean Nd isotope fingerprint must developed at a later point in the Neogene.

## Data availability

The datasets to this article are available in the Supplement.

## Declaration of Competing Interest

The authors declare that they have no known competing financial interests or personal relationships that could have appeared to influence the work reported in this paper.

## Acknowledgments

This research used samples provided by the International Ocean Discovery Program (IODP). We acknowledge the staff and shipboard party from Legs 28 and 29. We thank the staff at the Gulf Coast core repository (GCR) for curating these cores and assistance in core handling and shipping. We also acknowledge the Paleomagnetic Laboratory of Barcelona (CSIC-CCITUB). We also thank Denise Kulhanek and an anonymous reviewer for their constructive comments, which improved this paper. Funding to this research is provided by the Alexander S. Onassis Public Benefit Foundation Ph.D. research grant: F ZL 016-1/2015-2016; the Spanish Ministry of Economy, Industry and Competitiveness (grants CTM2017-89711-C2-1/2-P), co-funded by the European Union through FEDER funds; and an ECORD Research grant awarded to DE. PKB and FH acknowledge funding through the European Research Council starting grant #802835 OceaNice and NWO polar programme grant ALWPP2016.001. This paper is a contribution to the SCAR PAIS Programme.

## Appendix A. Supplementary data

Supplementary data to this article can be found online at <https://doi.org/10.1016/j.gloplacha.2021.103718>.

## References

Amakawa, H., Sasaki, K., Ebihara, M., 2009. Nd isotopic composition in the central North Pacific. *Geochim. Cosmochim. Acta* 73 (16), 4705–4719. <https://doi.org/10.1016/j.gca.2009.05.058>.  
Amakawa, Hiroshi, Yu, Tsai-Luen, Tazoe, Hirofumi, Obata, Hajime, Gamou, Toshitaka, Sano, Yuji, Shen, Chuan-Chou, Suzuki, Katsuhiko, 2019. Neodymium concentration

and isotopic composition distributions in the southwestern Indian Ocean and the Indian sector of the Southern Ocean. *Chemical Geology* 511, 190–203. <https://doi.org/10.1016/j.chemgeo.2019.01.007>.  
Basak, C., Pahnke, K., Frank, M., Lamy, F., Gersonde, R., 2015. Neodymium isotopic characterization of Ross Sea Bottom Water and its advection through the southern South Pacific. *Earth Planet. Sci. Lett.* 419, 211–221. <https://doi.org/10.1016/j.epsl.2015.03.011>.  
Bijl, P.K., Bendle, A.P.J., Bohaty, S.M., Pross, J., Schouten, S., Tauxe, L., Stickley, C.E., McKay, R.M., Röhl, U., Olney, M., Slujs, A., Escutia, C., Brinkhuis, H., Expedition 318 scientists, 2013. Eocene cooling linked to early flow across the Tasmanian Gateway. *P. Natl. Acad. Sci. USA* 110, 9645–9650.  
Bijl, P.K., Houben, A.J.P., Hartman, J.D., Pross, J., Salabarnada, A., Escutia, C., Sangiorgi, F., 2018. Paleocceanography and ice sheet variability offshore Wilkes Land, Antarctica – Part 2: Insights from Oligocene–Miocene dinoflagellate cyst assemblages. *Clim. Past* 14, 1015–1033. <https://doi.org/10.5194/cp-14-1015-2018>.  
Biscaye, P.E., 1965. Mineralogy and sedimentation of recent deep-sea clay in the Atlantic Ocean and adjacent seas and oceans. *Geol. Soc. Am. Bull.* 76 (7), 803–832.  
Bohaty, S.M., Zachos, J.C., Delaney, M.L., 2012. Foraminiferal Mg/ca evidence for Southern Ocean cooling across the Eocene-Oligocene transition. *Earth Planet. Sci. Lett.* 317–318 (2012), 251–261.  
Borg, S.G., Depaolo, D.J., Smith, B.M., 1990. Isotopic structure and tectonics of the central Transantarctic Mountains. *J. Geophys. Res. Solid Earth* 95 (B5), 6647–6667.  
Carter, L., McCave, I.N., 1997. The sedimentary regime beneath the deep western boundary current inflow to the Southwest Pacific Ocean. *J. Sediment. Res.* 67, 1005–1017.  
Chavagnac, V., Milton, J., Green, D., Breuer, J., Bruguier, O., Jacob, D., Jong, T., Kamenov, G., Le Huray, J., Liu, Y., 2007. Towards the development of a fossil bone geochemical standard: an inter-laboratory study. *Anal. Chim. Acta* 599 (2), 177–190.  
Conway, C.E., Bostock, H.C., Baker, J.A., Wysoczanski, R.J., Verdier, A., 2012. Evolution of Macquarie Ridge complex seamounts: Implications for volcanic and tectonic processes at the Australia-Pacific plate boundary south of New Zealand. *Mar. Geol.* 295–298, 34–50. <https://doi.org/10.1016/j.margeo.2011.11.009>.  
Cook, C.P., van de Fliedert, T., Williams, T., Hemming, S.R., Iwai, M., Kobayashi, M., Jimenez-Espejo, F.J., Escutia, C., Gonzalez, J.J., Khim, B.-K., McKay, R.M., Passchier, S., Bohaty, S.M., Riesselman, C.R., Tauxe, L., Sugisaki, S., Galindo, A.L., Patterson, M.O., Sangiorgi, F., Pierce, E.L., Brinkhuis, H., Klaus, A., Fehr, A., Bendle, J.A.P., Bijl, P.K., Carr, S.A., Dunbar, R.B., Flores, J.A., Hayden, T.G., Katsuki, K., Kong, G.S., Nakai, M., Olney, M.P., Pekar, S.F., Pross, J., Röhl, U., Sakai, T., Shrivastava, P.K., Stickley, C.E., Tuo, S., Welsh, K., Yamane, M., 2013. Dynamic behaviour of the East Antarctic ice sheet during Pliocene warmth. *Nat. Geosci.* 6 (9), 765–769. <https://doi.org/10.1038/ngeo1889>.  
Dalziel, I.W.D., 2014. Drake Passage and the Scotia arc: a tortuous space-time gateway for the Antarctic Circumpolar current. *Geology* (2014) 42 (4), 367–368. <https://doi.org/10.1130/focus042014.1>.  
Dijkstra, A.H., Sergeev, D.S., Spandler, C.A., Pettke, T., Meisel, T., Cawood, P.A., 2009. Highly refractory peridotites on Macquarie Island and the case for anciently depleted domains in the Earth's mantle. *J. Petrol.* 51 (1–2), 469–493. <https://doi.org/10.1093/ptrology/egp084>.  
Elderfield, H., Pagett, R., 1986. Rare earth elements in ichthyoliths: variations with redox conditions and depositional environment. *Sci. Total Environ.* 49, 175–197.  
Evangelinos, D., Escutia, C., Etourneau, J., Hoem, F., Bijl, P., Boterblom, W., van de Fliedert, T., Valero, L., Flores, J.A., Rodriguez-Tovar, F., Jimenez-Espejo, F., Salabarnada, A., López-Quirós, A., 2020. *Glob. Planet. Chang.* 191, 103221 <https://doi.org/10.1016/j.gloplacha.2020.103221>.  
Freslon, N., Bayon, G., Toucanne, S., Bermell, S., Bollinger, C., Chéron, S., Etoubleau, J., Germain, Y., Khrifounoff, A., Ponzevera, E., 2014. Rare earth elements and neodymium isotopes in sedimentary organic matter. *Geochim. Cosmochim. Acta* 140, 177–198. <https://doi.org/10.1016/j.gca.2014.05.016>.  
Galeotti, S., DeConto, E., Naish, T., Stocchi, P., Florindo, F., Pagani, M., Barrett, P., Bohaty, S.M., Lanci, L., Pollard, D., Sandroni, S., Malarico, F.M., Zachos, J.C., 2016. Antarctic Ice Sheet variability across the Eocene-Oligocene boundary climate transition. *Science* 352 (6281), 76–80. <https://doi.org/10.1126/science.aab0669>.  
García-Solsona, E., Jeandel, C., Labatut, M., Lacan, F., Vance, D., Chavagnac, V., Pradoux, C., 2014. Rare earth elements and Nd isotopes tracing water mass mixing and particle-seawater interactions in the SE Atlantic. *Geochim. Cosmochim. Acta* 125, 351–372. <https://doi.org/10.1016/j.gca.2013.10.009>.  
Gordon, A.L., Orsi, A.H., Muench, R., Huber, B.A., Zambianchi, E., Visbeck, M., 2009. Western Ross Sea continental slope gravity currents. *Deep-Sea Res. II* 56, 796–817.  
Gradstein, F.M., Ogg, J.G., Schmitz, M.D., Ogg, G.M., 2012. *The Geologic Time Scale 2012*. The Geol. Time Scale 2012 (2), 437–1144.  
Hartman, J.D., Sangiorgi, F., Salabarnada, A., Peterse, F., Houben, A.J.P., Schouten, S., Escutia, C., Bijl, P.K., 2018. Paleocceanography and Ice Sheet Variability Offshore Wilkes Land, Antarctica – Part 3: Insights from Oligocene – Miocene TEX 86 -Based Sea Surface Temperature Reconstructions, pp. 1275–1297.  
Hayes, D.E., Frakes, L.A., 1975. General synthesis, deep sea drilling project leg 28. In: *Initial Reports of the Deep Sea Drilling Project*, US, 28, pp. 19–48.  
Herold, N., Huber, M., Müller, R.D., Seton, M., 2012. Modeling the Miocene Climatic Optimum: Ocean Circulation, 27, pp. 1–22. <https://doi.org/10.1029/2010PA002041> (December 2011).  
Hill, D.J., Haywood, A.M., Valdes, P.J., Francis, J.E., Lunt, D.J., Wade, B.S., Bowman, V. C., 2013. Paleogeographic controls on the onset of the Antarctic circumpolar current. *Geophys. Res. Lett.* 40, 5199–5204. <https://doi.org/10.1002/grl.50941>.  
Hoem, F.S., Valero, L., Evangelinos, D., Escutia, C., Duncan, B., McKay, R.M., Brinkhuis, H., Sangiorgi, F., Bijl, P., 2021. Temperate Oligocene surface ocean conditions offshore Cape Adare, Ross Sea, Antarctica. *Clim. Past* 17, 1423–1442. <https://doi.org/10.5194/cp-17-1423-2021>.



- Huber, M., Brinkhuis, H., Stickley, C.E., Döös, K., Sluijs, A., Warnaar, J., Schellenberg, S. A., Williams, G.L., 2004. Eocene circulation of the Southern Ocean: was Antarctica kept warm by subtropical waters? *Paleoceanography* 19. <https://doi.org/10.1029/2004PA001014>.
- Huck, C.E., van de Flierdt, T., Jiménez-Espejo, F.J., Bohaty, S.M., Röhl, U., Hammond, S. J., 2016. Robustness of fossil fish teeth for seawater neodymium isotope reconstructions under variable redox conditions in an ancient shallow marine setting. *Geochem. Geophys. Geosyst.* 17 <https://doi.org/10.1002/2015GC006218>.
- Huck, C.E., van de Flierdt, T., Bohaty, S.M., Hammond, S.J., 2017. Antarctic climate, Southern Ocean circulation patterns, and deep water formation during the Eocene. *Paleoceanography* 32, 674–691. <https://doi.org/10.1002/2017PA003135>.
- Jacobsen, S.B., Wasserburg, G.J., 1980. Sm-Nd evolution of chondrites. *Earth Planet. Sci. Lett.* 50, 139–155. [https://doi.org/10.1016/0012-821X\(80\)90125-9](https://doi.org/10.1016/0012-821X(80)90125-9).
- Kennett, J.P., Houtz, R.E., Andrews, P.B., Edwards, A.R., Gostin, V.A., Hajos, M., Hampton, M., Jenkins, D.G., Margolis, S.V., Owenshine, A.T., Perch-Nielsen, K., 1975. Cenozoic paleoceanography in the Southwest Pacific Ocean, Antarctic glaciation, and the development of the Circum-Antarctic Current. *Initial Rep. Deep Sea Drill. Proj.* 29, 1155–1169.
- Kulhanek, D.K., Levy, R.H., Clowes, C.D., Prebble, J.G., Rodelli, D., Jovane, L., Morgans, H.E., Kraus, C., Zwingmann, H., Griffith, E.M., 2019. Revised chronostratigraphy of the RSDP Site 270 and late Oligocene to early Miocene paleoecology of the Ross Sea sector of Antarctica. *Glob. Planet. Chang.* 178, 46–64. <https://doi.org/10.1016/j.gloplacha.2019.04.002>.
- Lambelet, M., van de Flierdt, T., Crocket, K., Rehkämper, M., Kreissig, K., Coles, B., et al., 2016. Neodymium isotopic composition and concentration in the western North Atlantic Ocean: results from the GEOTRACES GA02 section. *Geochim. Cosmochim. Acta* 177, 1–29. <https://doi.org/10.1016/j.gca.2015.12.019>.
- Lambelet, M., van de Flierdt, T., Butler, E.C.V., Bowie, A.R., Rintoul, S.R., Watson, R.J., Remenyi, T., Lannuzel, D., Warner, M., Robinson, L.F., Bostock, H.C., Bradtmiller, L. I., 2018. The neodymium isotope fingerprint of Adélie Coast Bottom Water. *Geophys. Res. Lett.* 45, 11247–11256. <https://doi.org/10.1029/2018GL080074>.
- Levy, R.H., Meyers, S.R., Naish, T.R., Gollledge, N.R., McKay, R.M., Crampton, J.S., DeConto, R.M., De Santis, L., Florindo, F., Gasson, E.G.W., Harwood, D.M., Luyendyk, B.P., Powell, R.D., Clowes, C., Kulhanek, D.K., 2019. Antarctic ice-sheet sensitivity to obliquity forcing enhanced through ocean connections. *Nat. Geosci.* 12, 132–137.
- Martin, E.E., Haley, B.A., 2000. Fossil fish teeth as proxies for seawater Sr and Nd isotopes. *Geochim. Cosmochim. Acta* 64, 835–847. [https://doi.org/10.1016/S0016-7037\(99\)00376-2](https://doi.org/10.1016/S0016-7037(99)00376-2).
- McKinley, C.C., Thomas, D.J., LeVay, L., Rolewicz, Z., 2019. Nd isotopic structure of the Pacific Ocean 40–10 Ma, and evidence for the reorganization of deep North Pacific Ocean circulation between 36 and 25 Ma. *Earth Planet. Sci. Lett.* 521 (2019), 139–149.
- Müller, R.D., Seton, M., Zahirovic, S., Williams, S.E., Matthews, K.J., Wright, N.M., Shephard, G.E., Maloney, K., Barnett-Moore, N., Hosseinpour, M., 2016. Ocean Basin Evolution and Global-Scale Plate Reorganization events since Pangea Breakup. *Annu. Rev. Earth Planet. Sci.* 44 (1).
- Müller, R.D., Cannon, J., Qin, X., Watson, R.J., Gurnis, M., Williams, S., et al., 2018. GPlates: building a virtual Earth through deep time. *Geochem. Geophys. Geosyst.* 19 <https://doi.org/10.1029/2018GC007584>.
- Naish, T.R., Wilson, G.S., Dunbar, G.B., Barrett, P.J., 2008. Constraining the amplitude of late Oligocene bathymetric changes in western Ross Sea during orbitally-induced oscillations in the East Antarctic Ice Sheet: (2) implications for global sea-level changes. *Palaeogeogr. Palaeoclimatol. Palaeoecol.* 260, 66–76. <https://doi.org/10.1016/j.palaeo.2007.08.021>.
- Nelson, C.S., Cooke, P.J., 2001. History of oceanic front development in the new Zealand sector of the southern ocean during the cenozoic—a synthesis. *N. Z. J. Geol. Geophys.* 44 (4), 535–553. <https://doi.org/10.1080/00288306.2001.9514954>.
- Orsi, A.H., Whitworth, T., Nowlin, W.D., 1995. On the meridional extent and fronts of the antarctic circumpolar current. *Deep-Sea Res. Pt. I* 42, 641–673. [https://doi.org/10.1016/0967-0637\(95\)00021-W](https://doi.org/10.1016/0967-0637(95)00021-W).
- Pickett, D.A., Wasserburg, G.J., 1989. Neodymium and strontium isotopic characteristics of New Zealand granitoids and related rocks. *Contrib. Mineral. Petrol.* 103, 131–142.
- Rickli, J., Gutjahr, M., Vance, D., Fischer-Gödde, M., Hillenbrand, C.-D., Kuhn, G., 2014. Neodymium and hafnium boundary contributions to seawater along the West Antarctic continental margin. *Earth Planet. Sci. Lett.* 394, 99–110. <https://doi.org/10.1016/j.epsl.2014.03.008>.
- Rintoul, S.R., 1998. On the Origin and Influence of Adélie Land Bottom Water. In *Ocean, Ice, and Atmosphere: Interactions at the Antarctic Continental Margin*, vol. 75. American Geophysical Union, Washington, DC, pp. 151–171.
- Rintoul, S.R., 2018. The global influence of localized dynamics in the Southern Ocean. *Nature* 558 (7709), 209–218. <https://doi.org/10.1038/s41586-018-0182-3>.
- Rintoul, S.R., Sokolov, S., Williams, M.J.M., Peña Molino, B., Rosenberg, M., Bindoff, N. L., 2014. Antarctic Circumpolar current transport and barotropic transition at Macquarie Ridge. *Geophys. Res. Lett.* 41, 7254–7261. <https://doi.org/10.1002/2014GL061880>.
- Roberts, A.P., Sagnotti, L., Florindo, F., Bohaty, S.M., Verosub, K.L., Wilson, G.S., Zachos, J.C., 2013. Environmental record of paleoclimate, unroofing of the Transantarctic Mountains, and volcanism in later Eocene to early Miocene glacial marine sediments from the Victoria Land Basin, Ross Sea, Antarctica. *J. Geophys. Res. Solid Earth* 118 (1845–186), 1.
- Salabarnada, A., Escutia, C., Röhl, U., Nelson, C.H., McKay, R., Jiménez-Espejo, F.J., Bijl, P.K., Hartman, J.D., Strother, S.L., Salzmann, U., Evangelinos, D., López-Quiros, A., Flores, J.A., Sangiorgi, F., Ikehara, M., Brinkhuis, H., 2018. Paleocirculation and ice sheet variability offshore Wilkes Land, Antarctica – part 1: Insights from late Oligocene astronomically paced contourite sedimentation. *Clim. Past* 14, 991–1014. <https://doi.org/10.5194/cp-14-991-2018>.
- Sangiorgi, F., Bijl, P.K., Passchier, S., Salzmann, U., Schouten, S., McKay, R., Cody, R.D., Pross, J., Van De Flierdt, T., Bohaty, S.M., Levy, R., Williams, T., Escutia, C., Brinkhuis, H., 2018. Southern Ocean warming and Wilkes Land ice sheet retreat during the mid-Miocene. *Nat. Commun.* 9, 317. <https://doi.org/10.1038/s41467-017-02609-7>.
- Sarkar, S., Basak, C., Martin, F., Berndt, C., Huuse, M., Badhani, S., Bailas, J., 2019. Late eocene onset of the proto-antarctic circumpolar current. *Sci. Rep.* 9, 10125. <https://doi.org/10.1038/s41598-019-46253-1>.
- Scher, H.D., 2014. Stacking PEAT; a stacked Nd isotope record for the Paleogene equatorial Pacific. *Società Geologica Italiana* 31, 191–192. <https://doi.org/10.3301/ROL.2014.115>.
- Scher, H.D., Martin, E.E., 2004. Circulation in the Southern Ocean during the Paleogene inferred from neodymium isotopes. *Earth Planet. Sci. Lett.* 228, 391–405.
- Scher, H.D., Bohaty, S.M., Zachos, J.C., et al., 2011. Two stepping into the icehouse: East Antarctic weathering during progressive ice-sheet expansion at the Eocene-Oligocene transition. *Geology* 39, 383–386.
- Scher, H.D., Whittaker, J., William, S., Latimer, J., Kordesch, W., Delaney, M., 2015. Onset of Antarctic circumpolar current 30 million years ago as Tasmanian Gateway aligned with westerlies. *Nature* 523, 580–583.
- Schlitzer, R., 2016. Ocean data view. Retrieved from [odv.awi.de](http://odv.awi.de). <https://doi.org/10.1182/blood-2012-03-418400>.
- Scotese, C.R., Wright, N., 2018. PALEOMAP Paleodigital Elevation Models (PaleoDEMS) for the Phanerozoic PALEOMAP Project. <https://www.earthbyte.org/paleodem-resouce-scotese-and-wright-2018>.
- Sokolov, S., Rintoul, S.R., 2007. Multiple jets of the Antarctic Circumpolar current south of Australia. *J. Phys. Oceanogr.* 37 (5), 1394–1412. <https://doi.org/10.1175/JPO3111.1>.
- Sorlien, C.C., Luyendyk, B.P., Wilson, D.S., Bartek, L.R., Diebold, J.B., 2007. Oligocene development of the West Antarctic Ice Sheet recorded in eastern Ross Sea strata. *Geology* 35, 467–470.
- Stichel, T., Frank, M., Rickli, J., Haley, B.A., 2012. The hafnium and neodymium isotope composition of seawater in the Atlantic sector of the Southern Ocean. *Earth Planet. Sci. Lett.* 317–318, 282–294. <https://doi.org/10.1016/j.epsl.2011.11.025>.
- Stichel, T., Pahnke, K., Duggan, B., Goldstein, S.L., Hartman, A.E., Paffrath, R., Scher, H. D., 2018. TAG Plume: Revisiting the Hydrothermal Neodymium Contribution to Seawater. *Front. Mar. Sci.* 5 <https://doi.org/10.3389/fmars.2018.00096>.
- Stickley, C.E., Brinkhuis, H., Schellenberg, S., Sluijs, A., Roehl, U., Fuller, M., Grauert, M., Huber, M., Warnaar, J., Williams, G.L., 2004. Timing and nature of the deepening of the Tasmanian Gateway. *Paleoceanography* 19, PA4027.
- Tachikawa, K., Athias, V., Jeandel, C., 2003. Neodymium budget in the modern ocean and paleo-oceanographic implications. *J. Geophys. Res. Oceans* (1978–2012) 108 (C8).
- Tanaka, T., Togashi, S., Kamioka, H., Amakawa, H., Kagami, H., Hamamoto, T., Yuhara, M., Orihashi, Y., Yoneda, S., Shimizu, H., Kunimaru, T., Takahashi, K., Yanagi, T., Nakano, T., Fujimaki, H., Shinjo, R., Asahara, Y., Tanimizu, M., Dragusanu, C., 2000. JNd1-1: a neodymium isotopic reference in consistency with LaJolla neodymium. *Chem. Geol.* 168, 279–281.
- Taylor, S.R., McLennan, S.M., 1985. *The Continental Crust: Its Composition and Evolution*, 312 Pp. Blackwell Scientific Publications, Oxford, U. K.
- Thomas, D.J., Korty, R., Huber, M., Schubert, J.A., Haines, B., 2014. Nd isotopic structure of the Pacific Ocean 70–30 Ma and numerical evidence for vigorous ocean circulation and ocean heat transport in a greenhouse world. *Paleoceanography* 29, 454–469.
- van de Flierdt, T., Griffiths, A.M., Lambelet, M., Little, S.H., Stichel, T., Wilson, D., 2016. Neodymium in the oceans: a global database, a regional comparison and implications for paleoceanographic research. *Philos. Trans. R. Soc. A* 374, 20150293.
- Weis, D., Kieffer, B., Maerschalk, C., Barling, J., de Jong, J., Williams, G.A., Hanano, D., Pretorius, W., Mattielli, N., Scoates, J.S., 2006. High-precision isotopic characterization of USGS reference materials by TIMS and MC-ICP-MS. *Geochem. Geophys. Geosyst.* 7 (8), Q08006.
- Wright, N., Scher, H.D., Seton, M., Huck, C.E., Duggan, B.D., 2018. Change in Southern Ocean circulation in the Indian Ocean from the eocene through late oligocene. *Paleoceanogr. Palaeoclimatol.* 33 (2), 152–167. <https://doi.org/10.1002/2017PA003238>.
- Zachos, J.C., Breza, J., Wise, S.W., 1992. Earliest Oligocene ice-sheet expansion on East Antarctica: Stable isotope and sedimentological data from Kerguelen Plateau. *Geology* 20, 569–573.